



Measurement of the cavity-loaded quality factor in superconducting radio-frequency systems with mismatched source impedance

Jin-Ying Ma¹ · Cheng-Ye Xu¹ · An-Dong Wu^{1,2} · Guo-Dong Jiang¹ · Yue Tao¹ · Zong-Heng Xue¹ · Long-Bo Shi¹ · Tian-Cai Jiang¹ · Zheng-Long Zhu¹ · Zi-Qin Yang^{1,2} · Zheng Gao^{1,2} · Lie-Peng Sun^{1,2} · Gui-Rong Huang^{1,2} · Feng Qiu^{1,2} · Yuan He^{1,2}

Received: 3 November 2022 / Revised: 7 May 2023 / Accepted: 16 May 2023 / Published online: 25 August 2023

© The Author(s), under exclusive licence to China Science Publishing & Media Ltd. (Science Press), Shanghai Institute of Applied Physics, the Chinese Academy of Sciences, Chinese Nuclear Society 2023

Abstract

The accurate measurement of parameters such as the cavity-loaded quality factor (Q_L) and half bandwidth ($f_{0.5}$) is essential for monitoring the performance of superconducting radio-frequency cavities. However, the conventional “field decay method” employed to calibrate these values requires the cavity to satisfy a “zero-input” condition. This can be challenging when the source impedance is mismatched and produce nonzero forward signals (V_f) that significantly affect the measurement accuracy. To address this limitation, we developed a modified version of the “field decay method” based on the cavity differential equation. The proposed approach enables the precise calibration of $f_{0.5}$ even under mismatch conditions. We tested the proposed approach on the SRF cavities of the Chinese Accelerator-Driven System Front-End Demo Superconducting Linac and compared the results with those obtained from a network analyzer. The two sets of results were consistent, indicating the usefulness of the proposed approach.

Keywords Loaded quality factor · Field decay method · Superconducting cavity · Mismatch · Calibration · Cavity differential equation · Measurement · Accelerator-driven system

1 Introduction

Driven by the growing demand for safe nuclear fuel post-treatment processes, the China initiative Accelerator-Driven System (CiADS) is being constructed as a clean solution for nuclear fission power sources [1–3]. To

showcase the potential of a high-power continuous wave (CW) proton beam for this project, the China ADS Front-End Demo Linac (CAFe) was built. This Linac is a 162.5 MHz superconducting (SC) radio-frequency (RF) machine operating in the CW mode and consists of both normal conducting (NC) and SC sections (Fig. 1). The NC section includes an ion source, low-energy beam transport line, RF quadrupole accelerator, and medium-energy beam transport line. Conversely, the SC section comprises SC accelerating units, including 23 SC half-wave resonator cavities assembled into four cryomodules (CM1–CM4) [4–7]. The commissioning tests conducted on CAFe in the CW mode with a current of 10 mA and energy of 20 MeV successfully demonstrated its ability to accelerate and transmit high-intensity beams.

For an SC cavity, the loaded quality factor (Q_L) reflects the consumption of the stored electromagnetic energy inside the cavity. In an ideal situation, in the absence of a beam passing through the cavity, Q_L indicates the power dissipation from the cavity wall owing to the surface resistance (termed Q_0 [8, 9]) and the power leakage from the

This work was supported by the project of Large Research Infrastructures “China initiative Accelerator-Driven System” (No. 2017-000052-75-01-000590), “Studies of intelligent LLRF control algorithms for superconducting RF cavities” (No. E129851YR0), and the National Natural Science Foundation of China (No. 12205344).

✉ An-Dong Wu
antonwoo@impcas.ac.cn

✉ Feng Qiu
qiufeng@impcas.ac.cn

¹ Institute of Modern Physics, Chinese Academy of Sciences, Lanzhou 730000, China

² School of Nuclear Science and Technology, University of Chinese Academy of Sciences, Beijing 100049, China

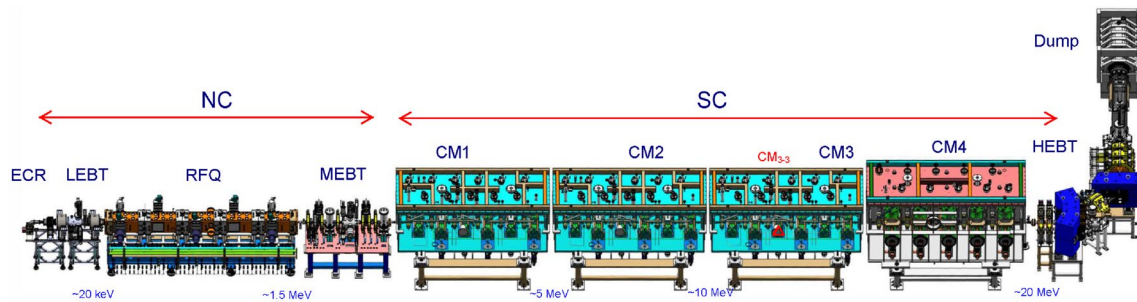


Fig. 1 (Color online) Layout of the CAFe facility. Two types of half-wave resonator superconducting cavities (HWR010 and HWR015) are implemented. The cavity CM_{3-3} is marked by a red triangle. Note

that for a cavity CM_{m-n} , the subscripts m and n represent the m^{th} cryomodule and n^{th} cavity, respectively

coupler ports (termed Q_e) [10]. Thus, Q_L is a critical parameter that must be carefully selected to match the impedance of the RF generator with the particle beam load during operation [11]. Furthermore, dark current loading can negatively affect Q_L , making it an important figure of merit for identifying such effects [12, 13]. In addition, Q_L (or the cavity half-bandwidth ($f_{0.5}$)) plays a crucial role in the design of model-based controllers [14–16]. To satisfy the aforementioned application requirements, the measurement error for Q_L should not exceed 5%. The value of Q_L can be calibrated using the cavity resonant frequency (f_0) and $f_{0.5}$, where $f_{0.5} = \frac{f_0}{2Q_L}$. Therefore, the precise measurement of $f_{0.5}$ is a prerequisite for calibrating Q_L . The decay curves of the cavity amplitude and phase (after the RF power is turned off) obtained from the cavity differential equation contain information on $f_{0.5}$ and the cavity detuning parameter (Δf), respectively. Many laboratories, including DESY, KEK, and CSNS, employ the “field decay method” to measure the aforementioned physical quantities [17–21].

We tracked the long-term changing regularity of $f_{0.5}$ based on the data obtained when the RF power was turned off and accumulated while the CAFe facility was operated. Occasionally, we found that the cavity half-bandwidth calculated using the amplitude decay curve (i.e., $f_{0.5,\text{decay}}$) and the cavity detuning parameter calculated using the phase decay curve (i.e., Δf_{decay}) appeared to be correlated. However, in principle, they should be independent. To better understand the above issue, we thoroughly examined the “field decay method”. Our findings revealed that this method is based on the zero-input response of the cavity differential equation, which indicates that the RF system must satisfy the “zero-input” condition. Thus, the cavity incident power must drop to zero after the RF power is turned off. However, if this condition is not met (i.e., owing to impedance mismatch), the remaining incident power may influence the decay process and render the “field decay method” ineffective. We constructed an equivalent circuit that included RF power

sources, transmission lines, input couplers, and SRF cavities and derived a solution for the cavity differential equation when a source impedance mismatch occurred. Finally, we modified the formula in the “field decay method” to explain the aforementioned correlation.

The “field decay method” is always employed to calibrate Q_L . If the aforementioned “zero-input” condition is not satisfied owing to impedance mismatch, considerable errors may occur in the measurement of Q_L . To improve measurement accuracy, this study focuses on a modified calibration algorithm based on an equivalent circuit.

2 Phenomena and possible interpretation

The conventional “field decay method” is briefly reviewed in this section. The naming rules for the cavity forward voltage signal (V_f) and cavity voltage (V_c) in polar coordinates are illustrated in Fig. 2. In polar coordinates, V_f and V_c can be expressed as $V_f = \frac{1}{2}\rho e^{i\theta}$ and $V_c = r e^{i\varphi}$, respectively, where ρ , r , θ , and φ represent the amplitudes of $2V_f$ and V_c and the phases of V_f and V_c , respectively.

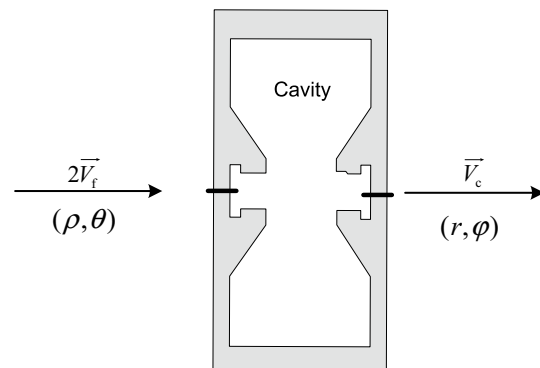


Fig. 2 Schematic interpreting the notations of the cavity differential equation in polar coordinates

When the RF power is turned off, ρ immediately decreases to zero in the ideal case. Under this condition, according to the SC cavity differential equation without the beam in polar coordinates [22–24], $f_{0.5}$ and Δf can be expressed as

$$\begin{cases} f_{0.5,\text{decay}} = -\left(\frac{r'}{r}\right) \cdot \frac{1}{2\pi} \\ \Delta f_{\text{decay}} = \frac{\phi'}{2\pi} \end{cases} \quad (1)$$

We refer to the various methods used in this study to calculate $f_{0.5}$ and Δf . For clarity, we first provide their detailed definitions in Table 1.

For the cavity CM_{3-3} (marked by a red triangle in Fig. 1) at CAFE, we measured the cavity-field decay curves for different values of Δf_{decay} (Fig. 3). f_0 was tuned using a frequency tuner. After the RF power was turned off, the slope of the cavity phase varied with the detuning parameter (Fig. 3c) because the phase decay curves are directly associated with the detuning parameter according to Eq. (1). Because the cavity Q_L is independent of the detuning parameter, the field decay curves of the cavity are expected to overlap under different detuning conditions; however, they appear to be affected by the detuning parameter (Fig. 3a and b). We conducted several studies to address this perplexing phenomenon.

First, we calibrated $f_{0.5,\text{decay}}$ and Δf_{decay} with four different values of V_c for the cavity CM_{3-3} (Fig. 4a). The value of V_c is less than the onset gradient of the field emission (approximately 1.2 MV). All four curves show the dependencies between $f_{0.5,\text{decay}}$ and Δf_{decay} . A similar dependence appears in another cavity (CM_{3-4}) (Fig. 4b).

Initially, we suspected that the frequency tuner might have disturbed the input coupler, causing variations in the coupling coefficients (β) and Q_L (or $f_{0.5,\text{decay}}$). Consequently, we turn off the tuner and achieve cavity detuning by scanning the frequency of the signal generator at the same CM_{3-3} . However, a similar dependence was observed in both cases (Fig. 4c. The deviation in Fig. 4c is primarily because of the slight differences in the cavity field levels.

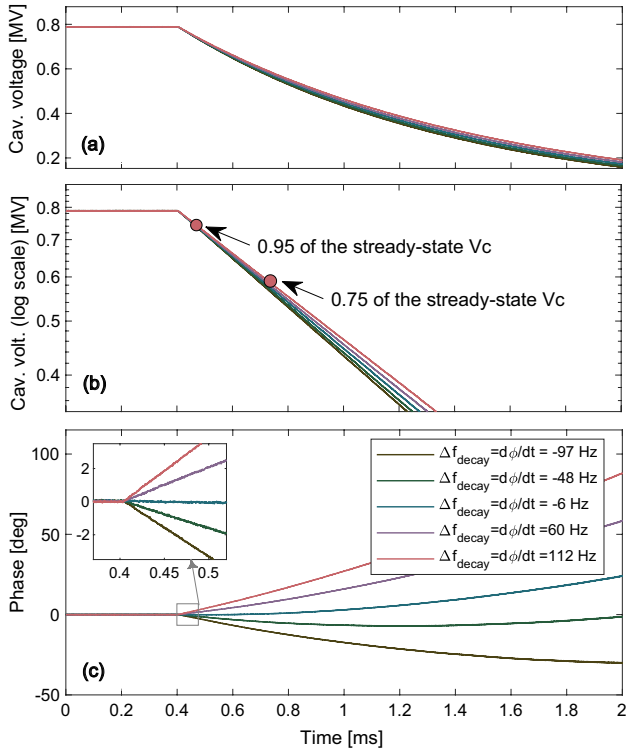


Fig. 3 (Color online) Cavity amplitude (a and b) and phase (c) decay curves before and after the RF power is turned off for various Δf on the cavity CM_{3-3} . The parameter $f_{0.5,\text{decay}}$ is obtained by calculating the slope of the decay curve between 0.95 and 0.75 of the steady-state V_c (see the middle plot)

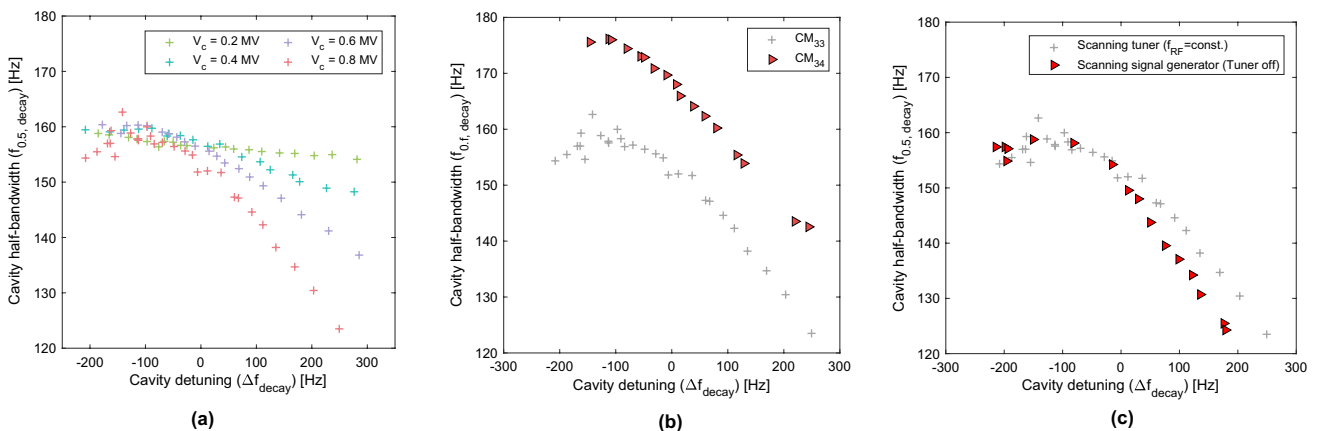


Fig. 4 a $f_{0.5,\text{decay}}$ and Δf_{decay} have dependency relations for different cavity voltages on CM_{3-3} , particularly when V_c is greater than 0.4 MV. b The dependency relations can also be observed in CM_{3-4} (red

triangles). c Comparison of the dependency relationships at CM_{3-3} when Δf_{decay} is scanned by the signal source (red triangles) and tuner (gray dots). The two curves exhibit the same tendency

Table 1 Definitions of the cavity-related notations

Notation	Definition
$f_{0.5}$	Actual cavity half bandwidth
$f_{0.5, \text{ decay}}$	Cavity half bandwidth calculated using the field decay curve with Eq. (1)
$f_{0.5, \text{ cali}}$	Cavity half bandwidth calibrated using Eq. (15)
$f_{0.5, \text{ scan}}$	Half bandwidth obtained by the network analyzer (scanning)
Δf	Actual cavity detuning
$\Delta f_{\text{ decay}}$	Cavity detuning calculated by the field decay curve with Eq. (1)
$\Delta f_{\text{ cali}}$	Cavity detuning calculated using Eq. (15)
$\Delta f_{\text{ ss}}$	Cavity detuning calculated from V_c and V_f in the steady-state

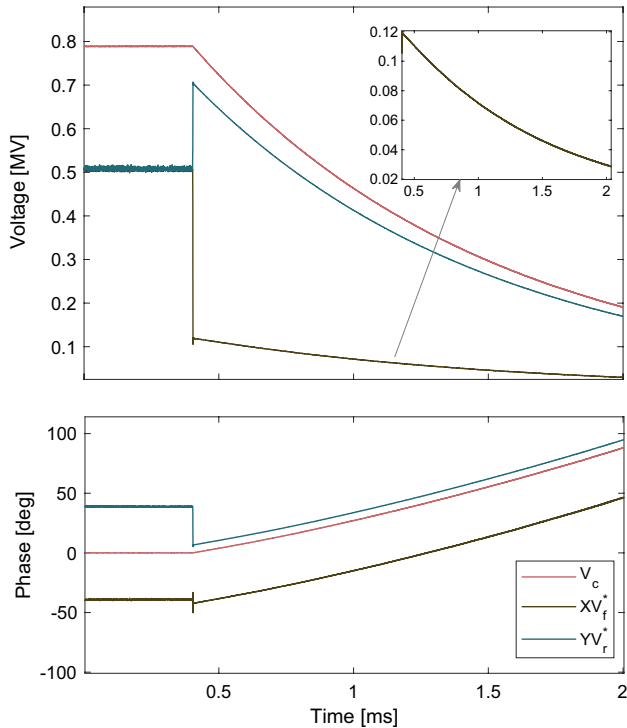


Fig. 5 (Color online) Voltage and phase of V_c , XV_f^* , and YV_r^* before and after turning off the RF power

Assuming that V_f^* and V_r^* represent the forward signal and reflected signal measured by the directional coupler, respectively, a further calibration of V_f^* and V_r^* is necessary to obtain the true forward and reflected signals (V_f and V_r) using $V_f = XV_f^*$ and $V_r = YV_r^*$, respectively (assuming that we neglect the channel crosstalk). The complex coefficients (X and Y) can be obtained by solving a linear regression equation [22]. Figure 5 compares the V_f , V_r and V_c signals, and a residual attenuation signal of V_f (i.e., XV_f^*) is observed after turning off the RF power. There are two possible reasons for this (Fig. 6).

1. The first reason is the crosstalk between the measurement channels, that is, the residual signal of V_f is coupled with

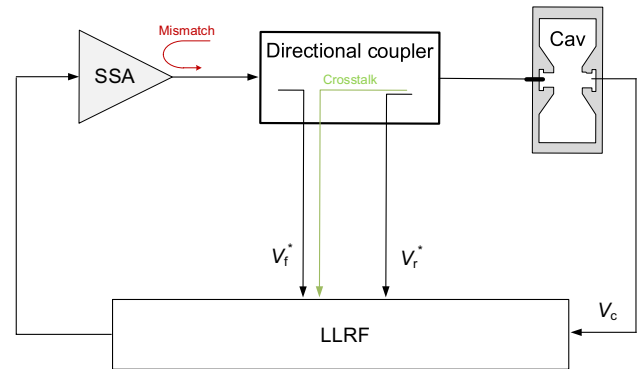


Fig. 6 Two causes of $V_r^* \neq 0$ (RF off): crosstalk between the measurement channels (green line) and source impedance mismatch (red line)

the signal V_r [22]. In this case, the residual signal is a false measurement signal.

2. The second reason is the source impedance mismatch, where the V_r signal is reflected from the generator side and mixed with the V_f signal. In this case, the residual signal is a true signal.

Before 2021, directional couplers with poor directivity (approximately 20 dB) were commonly used in our RF system, at CAFE facility. Previous studies have suggested that the limited directivity of these couplers was primarily responsible for the residual signals [24]. In 2022, we replaced all the old directional couplers with new ones exhibiting high directivity (40 dB). This resulted in almost negligible channel crosstalk; however, we decided not to install a high-power circulator in CAFE because of cost constraints. Based on these factors, we conclude that the residual V_f signal in Fig. 5 could be attributed to impedance mismatch rather than crosstalk.

The algorithm in Eq. (1) must be modified because the “zero-input” condition is not satisfied. The specific calibration algorithms are described in Sect. 3.

3 Theory and algorithm

In this section, we establish cavity differential equations for the mismatched source impedance condition and use them to derive new formulas for calibrating $f_{0.5}$ and Δf .

3.1 Radio-frequency and cavity circuit under the mismatched source impedance condition

Figure 7a presents a simplified model of an RF cavity coupled to an RF generator using a rigid coaxial line and an RF input power coupler [19]. In this model, the coaxial line is represented by a transmission line with a characteristic impedance (Z_0) and complex propagation constant ($\alpha + i\beta$). If the source impedance (Z_g) (on the generator side) is not equal to Z_0 , a portion of the cavity-reflected signal is measured by the direction coupler as the cavity forward signal after turning off the RF power. This process is described using an equivalent circuit (Fig. 7b). Assuming that the cavity input coupler has a transformation ratio of 1: N , the voltage signals V_c , V_f , and V_r , can be transformed into $V_c^\#$, $V_f^\#$, and $V_r^\#$, respectively, using the following transformation equation: $V^\# = \frac{1}{N} \cdot V$.

In Fig. 7b, the reflection coefficient (Γ_g) for the forward generator side at $z = 0$ can be expressed as [25]

$$\Gamma_g = \frac{V^-}{V^+} = \frac{Z_g - Z_0}{Z_g + Z_0}, \tag{2}$$

where V^+ and V^- represent the voltages of the incident and reflected waves at $z = 0$, respectively. After the RF power is turned off, the reflection coefficient at $z = -L$ (L is the length of the transmission line) is given by

$$\Gamma_L = \frac{V_f^\#}{V_r^\#} = \frac{V^- e^{-(\alpha+i\beta)L}}{V^+ e^{(\alpha+i\beta)L}} = \Gamma_g e^{-2(\alpha+i\beta)L}. \tag{3}$$

Therefore, after turning off the RF power, the transformed cavity voltage ($V_c^\#$) can be expressed as

$$V_c^\# = V_f^\# + V_r^\#. \tag{4}$$

Inserting Eq. (3) into Eq. (4) and eliminating $V_r^\#$, we obtain

$$V_f^\# = \frac{\Gamma_L}{1 + \Gamma_L} V_c^\#. \tag{5}$$

Accordingly, signal V_f is associated with signal V_c by

$$V_f = \frac{\Gamma_L}{1 + \Gamma_L} V_c. \tag{6}$$

In the absence of the beam current, the cavity differential equation can be expressed as:

$$\frac{dV_c}{dt} + (\omega_{0.5} - i\Delta\omega)V_c = \omega_{0.5}u, \tag{7}$$

and

$$u = \frac{2\beta_c}{\beta_c + 1} V_f. \tag{8}$$

Here, the parameter β_c is the coupling factor, which is generally considerably larger than 1 (i.e., $\beta_c \gg 1$). Thus, u can be simplified as $u = 2V_f$. By substituting V_f with Eq. (6) into Eq. (7), we obtain

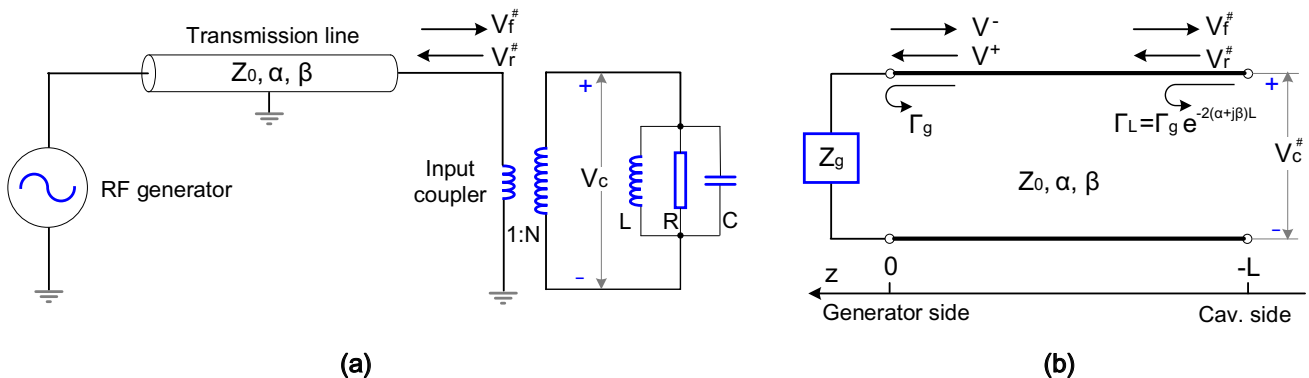


Fig. 7 **a** Simplified model of a cavity coupled to an RF generator by a rigid coaxial line and an RF input power coupler. **b** Equivalent circuit diagram of (a) after the RF power is turned off. The cavity voltage (V_c) is transformed into $V_c^\#$ on the left side of the input coupler

$$\frac{dV_c}{dt} + (\omega_{0.5} - i\Delta\omega)V_c = \omega_{0.5} \cdot \alpha \cdot V_c, \tag{9}$$

where $\alpha = 2\Gamma_L/(1 + \Gamma_L)$ denotes a complex factor. Equation (9) does not satisfy the “zero-input” condition. However, by rearranging the terms, we obtain an equation that satisfies the following condition:

$$\frac{dV_c(t)}{dt} + [\omega_{0.5}(1 - \alpha) - i\Delta\omega(t)]V_c(t) = 0. \tag{10}$$

3.2 New calibration algorithm for $f_{0.5}$ and Δf

It is more convenient to normalize the steady state ($V_c(t)$) to one, that is, $V_c(0) = 1$ if we assume that the RF power is turned off at $t = 0$ and the signal $V_c(t)$ is in steady state at $t \leq 0$. Under the aforementioned restrictions, the solution to Eq. (10) at $t \geq 0$ is given by:

$$V_c(t) = V_c(0)e^{\int_0^t [\omega_{0.5}(\alpha-1) + i\Delta\omega(\tau)]d\tau} = e^{\int_0^t [\omega_{0.5}(\alpha-1) + i\Delta\omega(\tau)]d\tau}. \tag{11}$$

The complex factor (α) can be decomposed into real and imaginary components (α_r and α_i), i.e., $\alpha = \alpha_r + i\alpha_i$.

Separating Eq. (11) into real and imaginary parts yields the following:

$$V_c(t) = e^{(\alpha_r-1)\omega_{0.5}t + i(\alpha_i\omega_{0.5}t + \int_0^t \Delta\omega(\tau)d\tau)}, (t \geq 0). \tag{12}$$

Consequently, the amplitude and phase of V_c are given by

$$\begin{cases} r = |V_c(t)| = e^{(\alpha_r-1)\omega_{0.5}t} \\ \varphi = \angle V_c(t) = \alpha_i\omega_{0.5}t + \int_0^t \Delta\omega(\tau)d\tau \end{cases} \tag{13}$$

Equation (13) provides some insights. If the source impedance (Z_g) perfectly matches the transmission line impedance (Z_0), then $\Gamma_g = 0$, $\Gamma_L = 0$, and $\alpha = 0$. In this scenario, according to the field decay algorithm, the cavity half bandwidth ($\omega_{0.5}$) and cavity detuning parameter ($\Delta\omega$) can be easily obtained by fitting the slope of the cavity amplitude and phase, i.e., $\omega_{0.5} = -r'/r$ and $\Delta\omega = \varphi'$. However, if the source impedance is not correctly matched to the transmission line ($\Gamma_g \neq 0$), the waves reflected from the cavity side will reflect again, resulting in nonzero forward power even after the RF power is turned off. This significantly affects the shape of the field curves, rendering the original algorithm inapplicable.

Using the original field decay method, the cavity half-bandwidth ($\omega_{0.5,decay}$) and detuning parameter ($\Delta\omega_{decay}$) were calibrated using

$$\begin{cases} \omega_{0.5,decay} = \frac{-r'}{r} = (1 - \alpha_r)\omega_{0.5} \\ \Delta\omega_{decay} = \varphi' = \alpha_i\omega_{0.5} + \Delta\omega \end{cases}. \tag{14}$$

To calibrate the actual cavity half-bandwidth and detuning parameters, the original algorithm must be modified as follows:

$$\begin{cases} f_{0.5,cali} = \frac{1}{2\pi} \cdot \frac{-r'/r}{1-\alpha_r} = \frac{f_{0.5,decay}}{1-\alpha_r} \\ \Delta f_{cali} = \frac{1}{2\pi} \varphi' - \alpha_i f_{0.5,cali} = \Delta f_{decay} - \alpha_i f_{0.5,cali} \end{cases}. \tag{15}$$

The estimation error of the original field-decay algorithm can be easily evaluated for a specified Γ_L . According to Eq. (15), the accuracies of $f_{0.5,decay}$ and Δf_{decay} can be expressed as:

$$\begin{cases} \frac{f_{0.5,decay} - f_{0.5,cali}}{f_{0.5,cali}} = -\alpha_r = -\Re\left(\frac{2\Gamma_L}{1+\Gamma_L}\right) \\ \frac{\Delta f_{decay} - \Delta f_{cali}}{f_{0.5,cali}} = \alpha_i = \Im\left(\frac{2\Gamma_L}{1+\Gamma_L}\right) \end{cases}. \tag{16}$$

The accuracy of the original field-decay algorithm depends on the parameter α , where the real (α_r) and imaginary (α_i) parts of α determine the accuracies of $f_{0.5,decay}$ and Δf_{decay} , respectively. Figure 8a and b illustrates the calibration errors of $f_{0.5,decay}$ and Δf_{decay} , respectively, as functions of Γ_L . To ensure that the accuracies of $f_{0.5,decay}$ and $\Delta f_{decay}/f_{0.5,cali}$ lie within the $\pm 5\%$ band, the coefficient Γ_L must be located inside the red circle (that is, $|\Gamma_L| < 0.024 \approx -32$ dB) in Fig. 8c. Figure 8d illustrates the specific relationship between the accuracies of $f_{0.5,decay}$, $\Delta f_{decay}/f_{0.5,cali}$ and Γ_L .

4 Modeling and simulation

The state-space formalism in Eq. (7) is given by [19, 26, 27]:

$$\frac{d}{dt} \begin{pmatrix} V_{c,r} \\ V_{c,i} \end{pmatrix} = \begin{pmatrix} -\omega_{0.5} & -\Delta\omega \\ \Delta\omega & -\omega_{0.5} \end{pmatrix} \begin{pmatrix} V_{c,r} \\ V_{c,i} \end{pmatrix} + \begin{pmatrix} \omega_{0.5} & 0 \\ 0 & \omega_{0.5} \end{pmatrix} \begin{pmatrix} u_r \\ u_i \end{pmatrix}. \tag{17}$$

Here, $V_{c,r}$ and $V_{c,i}$ represent the real and imaginary parts of the complex quantity (V_c), while u_r and u_i represent the real and imaginary parts of the complex quantity (u), respectively. Equation (17) can easily be transformed into its discrete-time form as follows [26, 27]:

$$\begin{bmatrix} V_{c,r}(n+1) \\ V_{c,i}(n+1) \end{bmatrix} = \begin{bmatrix} 1 - T_s\omega_{0.5} & -T_s\Delta\omega(n+1) \\ T_s\Delta\omega(n+1) & 1 - T_s\omega_{0.5} \end{bmatrix} \begin{bmatrix} V_{c,r}(n) \\ V_{c,i}(n) \end{bmatrix} + \begin{bmatrix} T_s\omega_{0.5} & 0 \\ 0 & T_s\omega_{0.5} \end{bmatrix} \begin{bmatrix} u_r(n) \\ u_i(n) \end{bmatrix}, \tag{18}$$

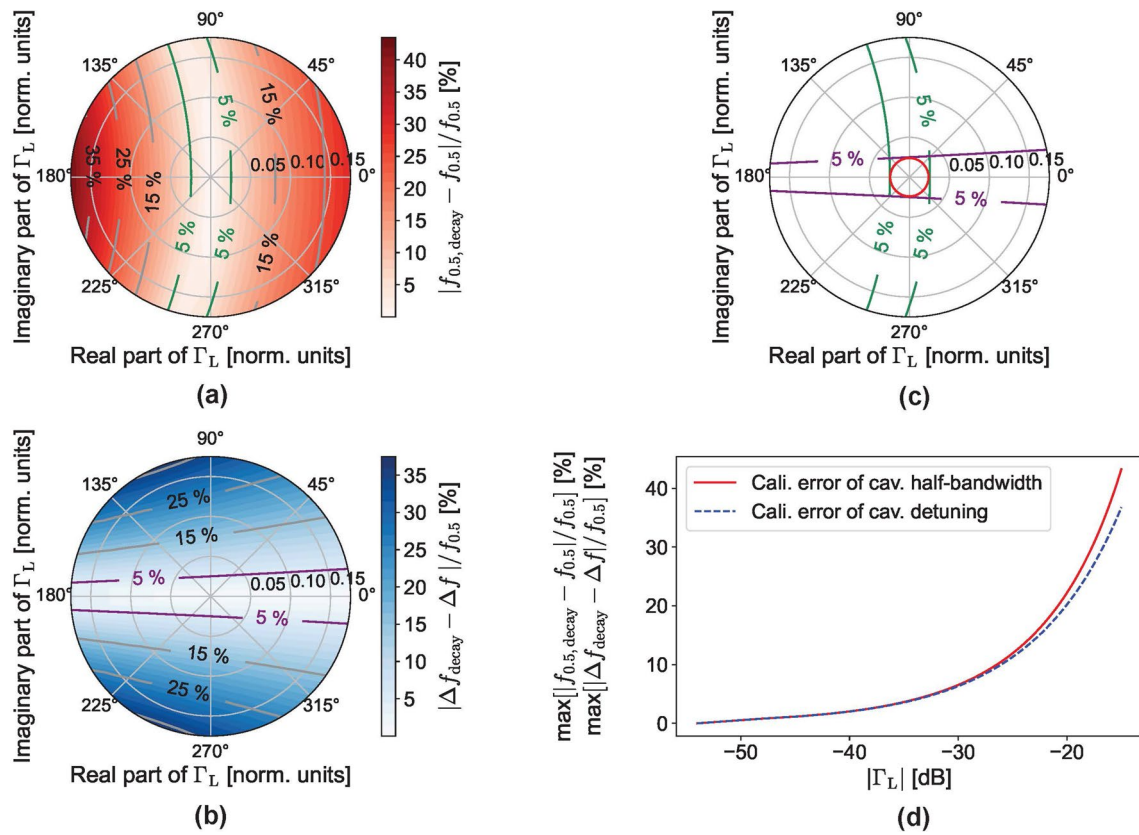


Fig. 8 (Color online) Calibration error of the cavity half bandwidth (a) and detuning parameter (b) as a function of the reflection coefficient (Γ_L), where Γ_L ranges from 0 to 0.18. The cavity bandwidth ($f_{0.5,decay}$) and Δf_{decay} are calibrated based on the field decay curves. To ensure that the accuracies of $f_{0.5,decay}$ and

$\Delta f_{decay}/f_{0.5,cali}$ lie within the $\pm 5\%$ band, Γ_L should be located inside the red circle (i.e., $|\Gamma_L| < 0.024 \approx -32$ dB), as illustrated in (c). The results in (d) show that the calibration error of $f_{0.5,decay}$ and Δf_{decay} increases with $|\Gamma_L|$, particularly when $|\Gamma_L|$ exceeds -32 dB

where T_s represents the sampling period. According to Eq. (9), the drive signal u can be expressed as

$$\begin{bmatrix} u_r(n+1) \\ u_i(n+1) \end{bmatrix} = \begin{bmatrix} \alpha_r & -\alpha_i \\ \alpha_i & \alpha_r \end{bmatrix} \begin{bmatrix} V_{c,r}(n+1) \\ V_{c,i}(n+1) \end{bmatrix}. \tag{19}$$

Other equations related to the dynamic behavior of the cavity are derived in Appendix A. The simulation parameters are presented in Table 2. After steady-state operation is achieved for 0.4 ms, the RF power is turned off. The signal reflected from the cavity is also reflected as Γ_g is not zero. Figure 9 compares the signals V_c , V_f , and V_r based on the cavity model (red dash line) and real SC cavity (thick solid gray line). The red dash lines and thick solid gray lines showed good consistency. In addition, the simulation results for the perfect impedance matching case ($\Gamma_g = 0$, indicated in green) are included for comparison.

According to Appendix A, the Lorentz force detuning (LFD) dynamics are assumed to be determined by a first-order differential equation. Consequently, the cavity phase

Table 2 RF and LFD parameters for the simulations

Item	Value
$f_{0.5}$ (Hz)	184
$\Delta f_{initial}$ (Hz)	149
$ \alpha $	0.31
$\angle \alpha$ (deg)	-42
τ_m (μ s)	530
L_{eff} (m)	0.038
K_{LFD} (Hz/(MV/m) ²)	0.15
T_s (ns)	80

signal presents curved trajectories (red dashed lines in Fig. 9) rather than linear trajectories. However, without the LFD dynamics, the cavity phase curve is linear, as indicated by the blue dotted lines in Fig. 9a. The slope of the linear phase curve represents the cavity detuning parameter ($\Delta\omega_{decay}$). The cavity phase curves overlap in the first 80 μ s after the RF power is turned off, regardless of whether the LFD is included (Fig. 9a). For clarity, the LFD dynamics

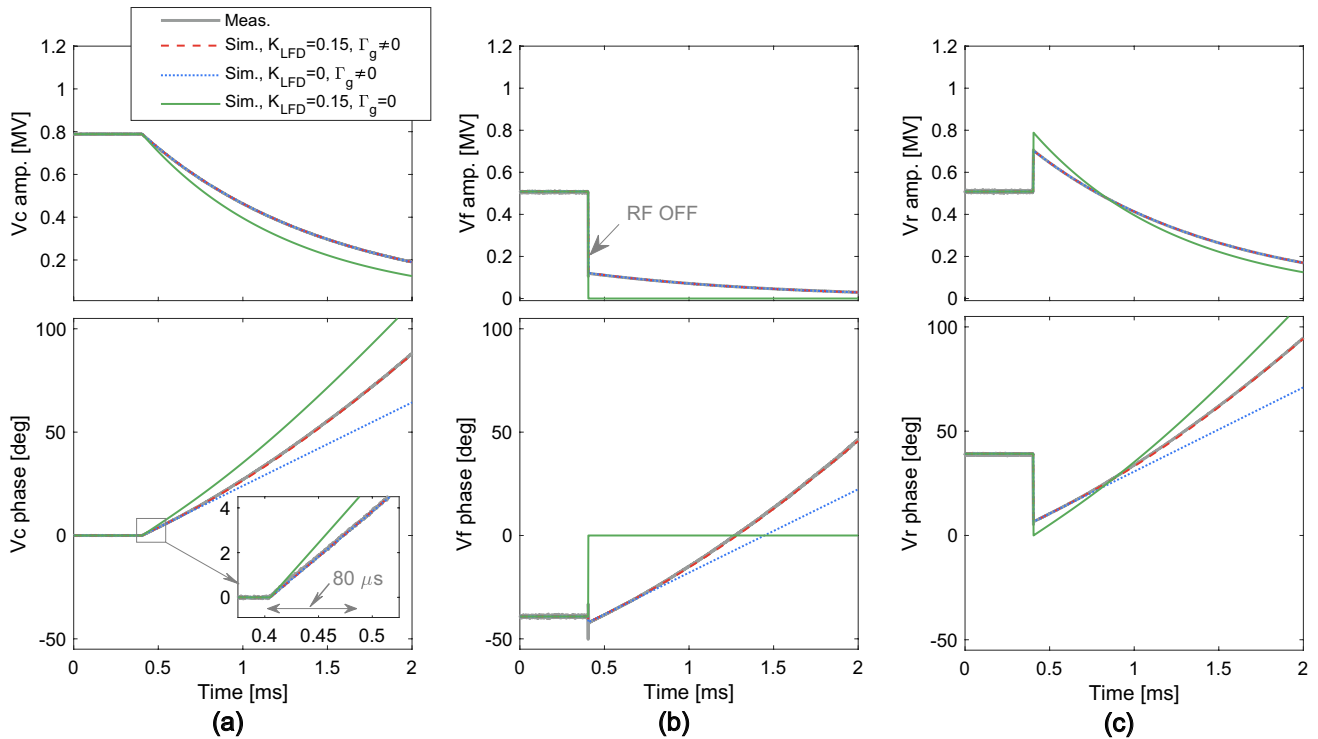


Fig. 9 (Color online) Comparison of the cavity voltage (a), cavity forward (b), and reflected signal (c) measurements based on the cavity model (red) and real SC cavity (gray). A stable operation is maintained for 0.4 ms before the RF power is turned off to create a field decay event. In the cavity model, the LFD dynamics is assumed to be determined by a first-order differential equation, resulting

in curved trajectories in the cavity phase signal (red dashed lines) instead of linear ones. When the LFD effect is neglected, the cavity phase curve is linear (blue dotted lines), as shown in (a). In addition, the simulation results for the perfect impedance match case ($\Gamma_g = 0$, indicated by green solid line) are also included for comparison

during the field decay process were examined (Fig. 10). For the subsequent 80 μs after the RF power is turned off, the LFD-induced phase error and maximum LFD value are less than 0.01 deg and approximately 0.8 Hz, respectively. Consequently, it is reasonable to fit the 80 μs cavity phase data to obtain Δf .

5 Experimental verification

Based on the algorithm in (15), we recalibrated the measurement results shown in Fig. 4a. The details of the process are described below.

1. Calibrating the actual forward and reflected signals using $V_f = XV_f^*$ and $V_r = XV_r^*$, respectively: The complex factors (X and Y) were determined by solving a linear regression equation [22].
2. Determining the factor α : According to (6), we calculated α as twice the ratio of V_f to V_c after turning off the RF power. Here, we averaged α over a time interval of 50 μs (e.g., from 0.45 ms to 0.5 ms in Fig. 11) to reduce uncertainty.

3. Calibrating $f_{0.5,\text{decay}}$ and Δf_{decay} using the traditional “field decay method”: To ensure a sufficient signal-to-noise ratio, we determined $f_{0.5,\text{decay}}$ by calculating the slope of the decay curve between 0.95 and 0.75 in the steady-state (V_c) (Fig. 3b). To avoid the LFD effect, we determined the derivative of the cavity phase within an 80 μs interval after the RF power was turned off to obtain Δf_{decay} .
4. Calibrating $f_{0.5,\text{cali}}$ and Δf_{cali} : We used the formula (15) with the known values of α , $f_{0.5,\text{decay}}$, and Δf_{decay} to calibrate $f_{0.5,\text{cali}}$ and Δf_{cali} .

We used the aforementioned procedure to calibrate $f_{0.5,\text{cali}}$ and Δf_{cali} (Fig. 12a). In contrast to the strong correlation observed between $f_{0.5,\text{decay}}$ and Δf_{decay} measured by the cavity amplitude and phase decay curve, the new calibrated value of $f_{0.5,\text{cali}}$ was not independent of Δf_{cali} at different V_c levels.

We also compared Δf_{cali} and Δf_{decay} with the steady-state cavity detuning parameters (Δf_{ss}), which were calculated from the steady-state values of V_f and V_c (Fig. 12b). The following expression was used to calibrate Δf_{ss} :

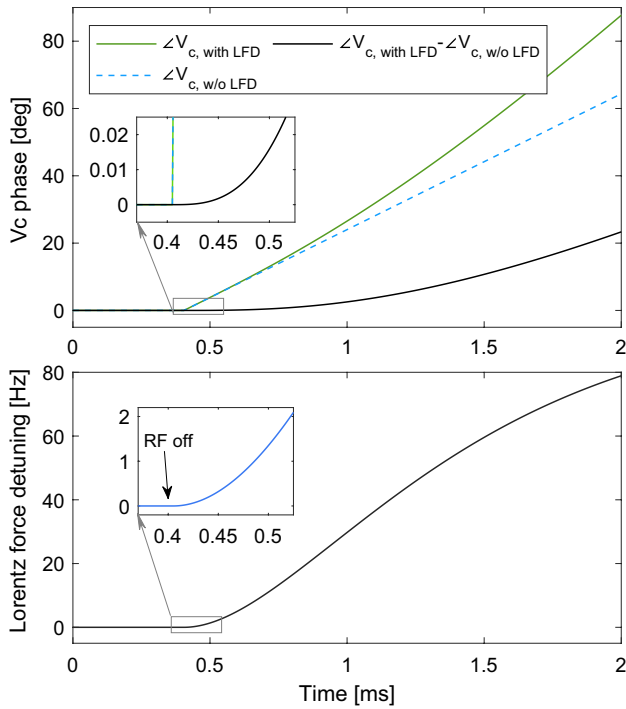


Fig. 10 Simulation results showing the effect of the LFD on the measurement accuracy of the cavity phase and cavity detuning. For the initial 80 μ s period after turning off the RF power, the LFD-induced phase error is less than 0.01 deg, which can be ignored

$$\Delta f_{ss} = \tan(\varphi - \theta) \cdot f_{0.5, \text{cali}} \quad (20)$$

Figure 12b indicates that the discrepancy between Δf_{cali} and Δf_{ss} is less than ± 5 Hz, whereas there is an offset of approximately 40 Hz between Δf_{decay} and Δf_{ss} .

To further validate the proposed algorithm, we used a network analyzer to measure CM_{3-3} and perform a comparison. Figure 13a and b shows the measurement setup, and the frequency-response measurement and corresponding fitted curve, respectively. The measurement results were fitted using the following formula

$$A_{\text{fit}} = \frac{A_{\text{max}} \cdot f_{0.5}}{\sqrt{(f - f_{\text{offset}})^2 + f_{0.5}^2}} \quad (21)$$

where A_{max} is the maximum value of the amplitude–frequency-response curve. The parameters f and f_{offset} represent the stimulus frequency and frequency offset between the cavity resonant frequency and RF, respectively. In Fig. 13b, the estimated value of $f_{0.5}$ for the fitted curve is 183.7 Hz.

Next, we utilized a network analyzer to scan the cavities in $CM_1 - CM_3$ and estimated $f_{0.5, \text{scan}}$ by curve fitting. We then compared the derivation between $f_{0.5, \text{cali}}$ and $f_{0.5, \text{scan}}$ for the 16 cavities (excluding CM_{2-6} and CM_{3-1} because of cavity faults). In addition, we plot the deviation between $f_{0.5, \text{decay}}$ and $f_{0.5, \text{scan}}$ for comparison purposes. The results are shown in Fig. 14. The deviation between $f_{0.5, \text{scan}}$ and $f_{0.5, \text{cali}}$ was maintained roughly within $\pm 2\%$, indicating that the proposed calibration algorithm accurately estimated the values of $f_{0.5}$

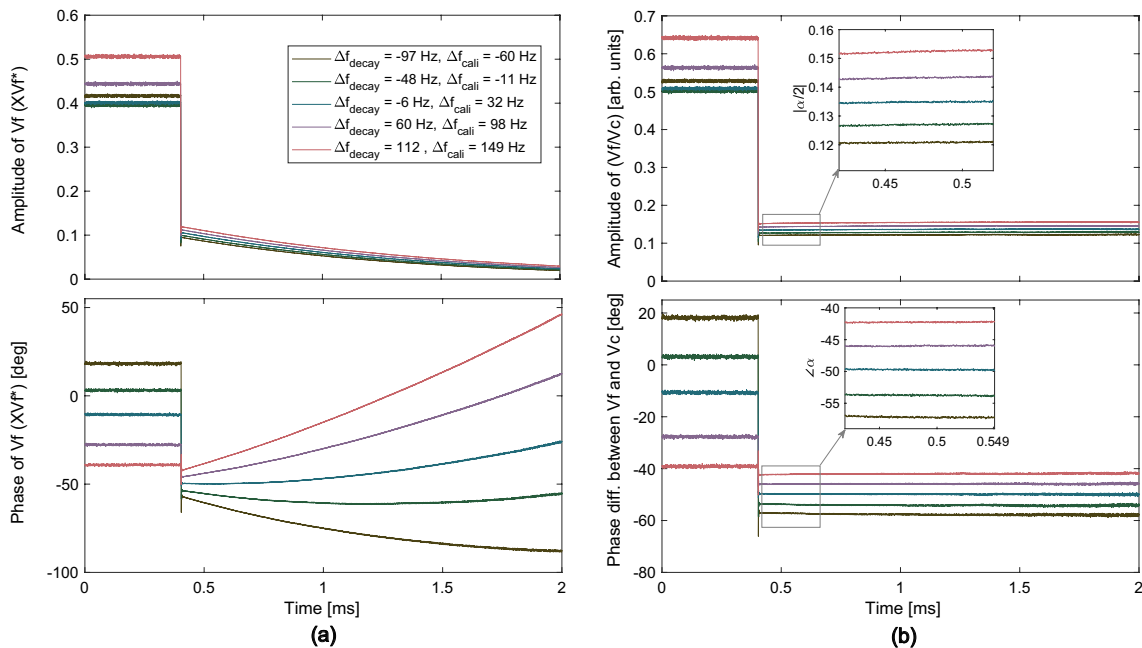


Fig. 11 **a** Cavity forward signal (V_f) for different detuning values on cavity CM_{3-3} (the corresponding cavity voltage signal is given in Fig. 3). **b** Method for estimating α from the V_c and V_f signals after the RF power is turned off

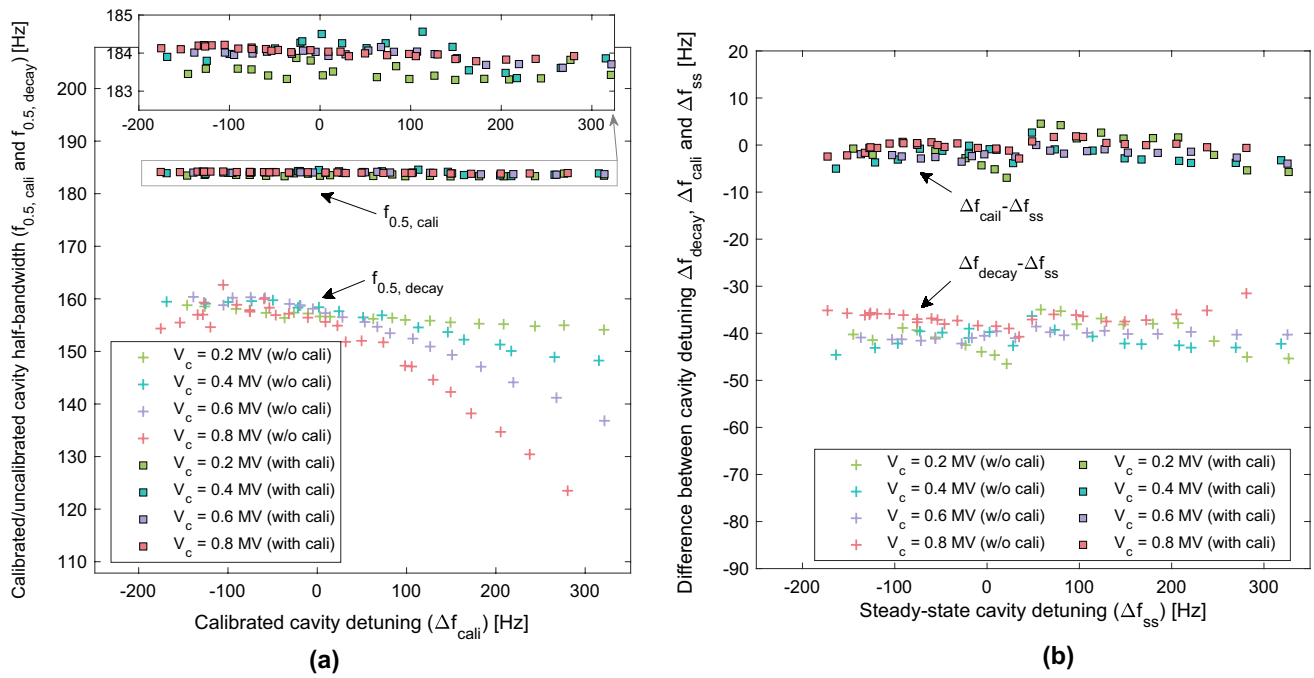
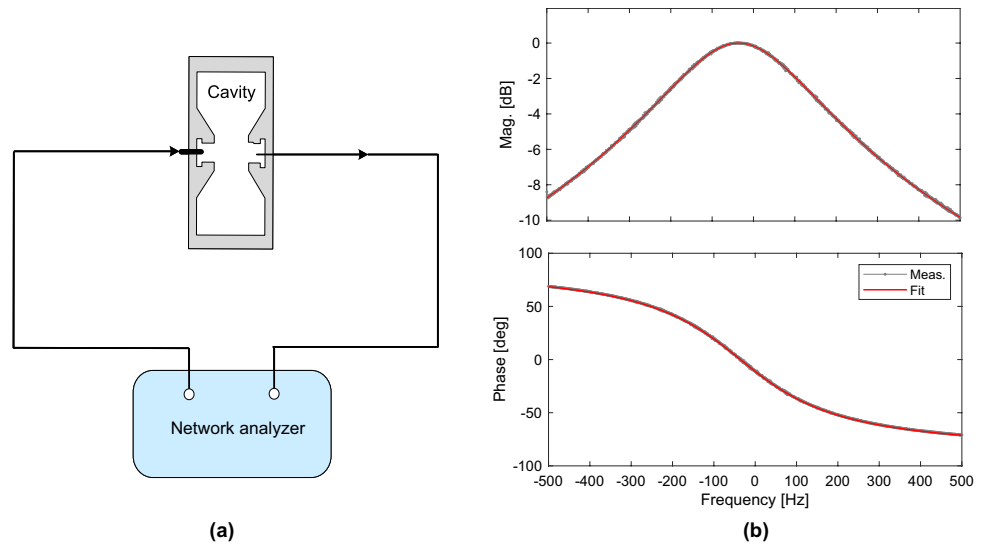


Fig. 12 (Color online) **a** Relationship between the cavity half bandwidth ($f_{0.5}$) and cavity detuning parameter (Δf_{cali}) in the calibrated and uncalibrated algorithms for various values of V_c . **b**

Comparison of the results of Δf_{decay} and Δf_{cali} measurements with the cavity detuning value (Δf_{ss}) obtained in the steady state

Fig. 13 a Measurement block diagram based on the network analyzer. **b** Frequency response function of cavity CM_{3-3} , as measured by the network analyzer. The f_{offset} parameter is excluded for better comparison



6 Conclusion

After the RF power was turned off, the residual signal (V_f) caused by source impedance mismatch could affect the field decay process, resulting in measurement errors for $f_{0.5}$ and Δf . The simulation results indicate that, to ensure that the measurement errors of $f_{0.5}$ and Δf were less than 5%, the reflection coefficient at the generator side

must be less than -32 dB. To improve the measurement accuracy, we derived a calibration algorithm based on the cavity differential equation for cases in which there was a source impedance mismatch. Using this algorithm, we recalibrated $f_{0.5}$ and Δf and compared the results with those obtained from network analyzer measurements. The maximum error between the calculated and measured values was within 2%.

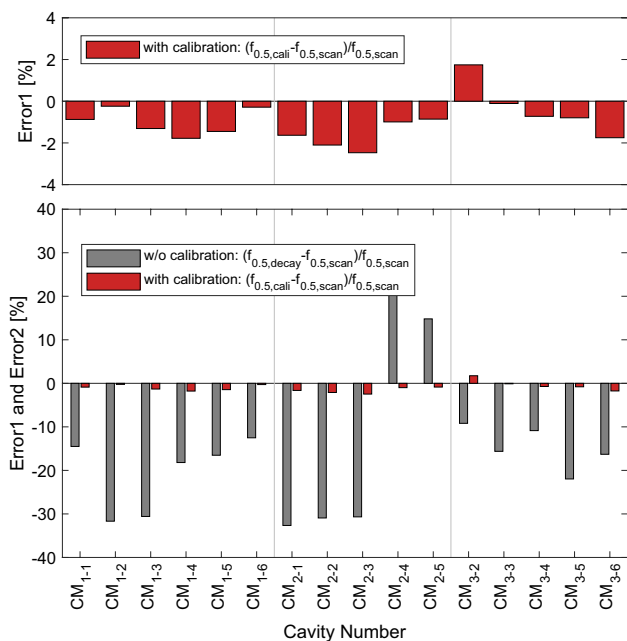


Fig. 14 Comparison of the deviation between $f_{0.5,decay}$ and $f_{0.5,cali}$ for the 16 cavities and the network analyzer measurement results, $f_{0.5,cali}$

α is a crucial factor in the calibration algorithm that ultimately depends on the impedance Z_g on the generator side. Unfortunately, we do not have a comprehensive understanding of the factors that determine Z_g . One possible factor is the power output of the RF generator. For instance, different V_c and detuning parameters require different RF powers, which lead to different Z_g values. Nevertheless, it is important to stress that Z_g is not determined solely by the generator power, and the same power may result in different values of Z_g . In our future work, we shall focus on identifying the mechanisms and physical quantities that affect Z_g .

Appendix A: dynamic behavior of the cavity

The LFD must be considered because the cavity gradient varies after the RF power is turned off. As the cavity field attenuates slowly owing to the high loaded Q (narrow bandwidth) characteristic, higher-order mechanical modes are usually not excited. In this case, the LFD dynamics can be described by a first-order differential equation [19] as follows:

$$\tau_m \frac{d}{dt} \Delta f_{LFD}(t) + \Delta f_{LFD}(t) = -K_{LFD} E_{peak}^2, \tag{22}$$

where K_{LFD} and τ denote the LFD coefficient and mechanical time constant, respectively. The quantity E_{peak} is the

cavity peak gradient, which can be defined as V_c using $E_{peak} = V_c / L_{eff}$, where L_{eff} is the effective cavity length.

According to Ref. [27], the corresponding difference equation of Eq. (22) is given by

$$\Delta f_{LFD}(n + 1) = b \Delta f_{LFD}(n) + g \left[V_{c,r}^2(n) + V_{c,i}^2(n) \right], \tag{23}$$

where the coefficients are $b = e^{-T_s/\tau_{LFD}}$ and $g = (1 - b) \frac{-K_{LFD}}{L_{eff}^2}$.

When the RF power is turned off, the cavity field exponentially decreases to zero. The corresponding LFD parameter value increases from its initial value of negative dozens (hundreds) of Hz to zero. In addition, we assume that LFD is the only dominant cavity detuning that occurs after the RF power is turned off (other sources may cause negligible detuning), and as V_c^2 varies from $V_c^2(0)$ to $V_c^2(t)$, the LFD dynamics can be modified as follows:

$$\Delta f_{LFD}(n + 1) = b \Delta f_{LFD}(n) + g \left[V_{c,r}^2(n) + V_{c,i}^2(n) - 1 \right]. \tag{24}$$

The constant 1 in Eq. (24) represents the square of the steady-state (V_c) amplitude, which is normalized to one for simplicity, that is, $V_{c,r}^2(0) + V_{c,i}^2(0) = 1$

Thus, the overall cavity detuning is given by:

$$\Delta \omega(n + 1) = 2\pi \left[\Delta f_{initial} + \Delta f_{LFD}(n + 1) \right]. \tag{25}$$

Here, $\Delta f_{initial}$ is the initial steady-state detuning parameter before the RF power source is turned off. Using the difference Eq. (17), (19), (24), and (25), a dynamic simulation of the cavity undergoing a complete field decay process can be easily performed.

Author's contributions All authors contributed to the study conception and design. Material preparation, data collection and analysis were performed by Feng Qiu, An-Dong Wu and Jin-Ying Ma. The first draft of the manuscript was written by Jin-Ying Ma, and all authors commented on previous versions of the manuscript. All authors read and approved the final manuscript.

Declarations

Conflict of interest Yuan He is an editorial board member for Nuclear Science and Techniques and was not involved in the editorial review, or the decision to publish this article. All authors declare that there are no competing interests.

References

1. W.L. Zhan, Accelerator driven sustainable fission energy. In: Proceedings of the 7th International Particle Accelerator Conference, IPAC2016, Busan, Korea, 2016. <https://doi.org/10.18429/JACoW-IPAC2016-FRYAA03>
2. Y.S. Qin, P. Zhang, H.J. Cai et al., Transfer line including vacuum differential system for a high-power windowless target. Phys. Rev.

- Accel. Beams **23**, 113002 (2020). <https://doi.org/10.1103/PhysRevAccelBeams.23.113002>
3. S.H. Liu, Z.J. Wang, H. Jia et al., Physics design of the CIADS 25 MeV demo facility. *Nucl. Instrum. Meth. A* **843**, 11–27 (2017). <https://doi.org/10.1016/j.nima.2016.10.055>
 4. Y. He, T. Tan, A.D. Wu, et al., Operation experience at CAFe. In: Oral Presentation of the 2021 International Conference on RF Superconductivity, SRF'21, in: virtual conference, JACoW, virtual conference. Available at: https://indico.frib.msu.edu/event/38/attachments/160/1298/MOOFV03_yuan_he.pdf (2021)
 5. Q. Chen, Z. Gao, Z.L. Zhu et al., Multi-frequency point supported LLRF front-end for CIADS wide-bandwidth application. *Nucl. Sci. Tech.* **31**, 29 (2020). <https://doi.org/10.1007/s41365-020-0733-9>
 6. W.M. Yue, S. X. Zhang, C. L. Li, et al., Design, fabrication and test of a taper-type half-wave superconducting cavity with the optimal beta of 0.15 at IMP. *Nucl. Eng. Technol.* **52**, 1777–1783 (2020). <https://doi.org/10.1016/j.net.2020.01.014>.
 7. W.M. Yue, S.X. Zhang, C.L. Li et al., Development of a low beta half-wave superconducting cavity and its improvement from mechanical point of view. *Nucl. Instrum. Meth. A* **953**, 163259 (2020). <https://doi.org/10.1016/j.nima.2019.163259>
 8. P. Sha, W.M. Pan, S. Jin et al., Ultrahigh accelerating gradient and quality factor of CEPC 650 MHz superconducting radio-frequency cavity. *Nucl. Sci. Tech.* **33**, 125 (2022). <https://doi.org/10.1007/s41365-022-01109-8>
 9. Z.Y. Ma, S.J. Zhao, X.M. Liu, et al. High RF power tests of the first 1.3 GHz fundamental power coupler prototypes for the SHINE project. *Nucl. Sci. Tech.* **33**, 10 (2022). <https://doi.org/10.1007/s41365-022-00984-5>
 10. J.P. Holzbauer, C. Contreras, Y. Pischalnikov et al., Improved RF measurements of SRF cavity quality factors. *Nucl. Instrum. Meth. A* **913**, 7–14 (2019). <https://doi.org/10.1016/j.nima.2018.09.155>
 11. F. Marhauser, Method for in situ and in operando cavity loaded Q extraction in superconducting rf accelerators. *Phys. Rev. Accel. Beams* **24**, 032001 (2021). <https://doi.org/10.1103/PhysRevAccelBeams.24.032001>
 12. A. Bellandi, Ł. Butkowski, B. Dursun et al., Online detuning computation and quench detection for superconducting resonators. *IEEE T. Nucl. Sci.* **68**, 385–393 (2021). <https://doi.org/10.1109/TNS.2021.3067598>.
 13. J. Branlard, V. Ayvazyan, O. Hensler, et al., Superconducting cavity quench detection and prevention for the European XFEL. In: Proceedings of ICALEPCS2013, San Francisco, CA, USA. Available at <https://accelconf.web.cern.ch/ICALEPCS2013/papers/thhppc072.pdf>
 14. F. Qiu, S. Michizono, T. Miura et al., Application of disturbance observer-based control in low-level radio-frequency system in a compact energy recovery linac at KEK. *Phys. Rev. ST Accel. Beams*. **18**, 092801 (2015). <https://doi.org/10.1103/PhysRevSTAB.18.092801>
 15. F. Qiu, S. Michizono, T. Matsumoto et al., Combined disturbance-observer-based control and iterative learning control design for pulsed superconducting radio frequency cavities. *Nucl. Sci. Tech.* **32**, 56 (2021). <https://doi.org/10.1007/s41365-021-00894-y>
 16. Y. Cong, S.F. Xu, W.X. Zhou et al., Low-level radio-frequency system upgrade for the IMP Heavy Ion Reach Facility in Lanzhou (HIRFL). *Nucl. Instrum. Meth. A* **925**, 76–86 (2019). <https://doi.org/10.1016/j.nima.2019.01.086>
 17. M. Omet, Digital low level RF control techniques and procedures towards the international linear collider (Ph.D. thesis). School of High Energy Accelerator Science (2014)
 18. F. Qiu, T. Miura, D. Arakawa et al., RF commissioning of the compact energy recovery linac superconducting cavities in pulse mode. *Nucl. Instrum. Meth. A* **985**, 164660 (2021). <https://doi.org/10.1016/j.nima.2020.164660>
 19. T. Schilcher, Ph.D. thesis, Universitt Hamburg (1998)
 20. J.Y. Ma, G.R. Huang, Z. Gao et al., The resonant frequency measurement method for superconducting cavity with Lorentz force detuning. *Nucl. Instrum. Meth. A* **993**, 165085 (2021). <https://doi.org/10.1016/j.nima.2021.165085>
 21. Z.C. Mu, Overview of the CSNS linac LLRF and operational experiences during beam commissioning.. In: Proceedings of the 57th ICFA Advanced Beam Dynamics Workshop on High-Intensity, High Brightness and High Power Hadron Beams, Malmö, Sweden, pp. 3–8 (2016)
 22. A. Brandt, Development of a finite state machine for the automated operation of the LLRF control at FLASH(Ph.D. thesis). University Hamburg (2007)
 23. M. Grecki, V. Ayvazyan, J. Branlard et al., On-line RF amplitude and phase calibration for vector sum control. In: Oral Presentation of the 9th Low-Level RF Workshop, LLRF2019, Chicago, USA September 29–October 3, (2019)
 24. F. Qiu, J.Y. Ma, G.D. Jiang et al., Approach to calibrate actual cavity forward and reflected signals for continuous wave-operated cavities. *Nucl. Instrum. Meth. A* **1034**, 166769 (2022). <https://doi.org/10.1016/j.nima.2022.166769>
 25. David, M. Pozar., *Microwave Engineering*, 4th Edition, Wiley
 26. T. Czarski, K.T. Pozniak, R.S. Romaniuk et al., TESLA cavity modeling and digital implementation in FPGA technology for control system development. *Nucl. Instrum. Methods A* **548**, 283 (2005). <https://doi.org/10.1016/j.nima.2005.10.122>
 27. F. Qiu, S. Michizono, T. Miura et al., Real-time cavity simulator based low-level radio frequency test bench and applications for accelerators. *Phys. Rev. Accel. Beams* **21**, 032003 (2018). <https://doi.org/10.1103/PhysRevSTAB.21.032003>

Springer Nature or its licensor (e.g. a society or other partner) holds exclusive rights to this article under a publishing agreement with the author(s) or other rightsholder(s); author self-archiving of the accepted manuscript version of this article is solely governed by the terms of such publishing agreement and applicable law.